UNIVERSITÀ DEGLI STUDI DI UDINE

Università degli studi di Udine

Analytical Procedure for the Extraction of Material Parameters in Antiferroelectric ZrO2

Original

Availability:
This version is available http://hdl.handle.net/11390/1245884 since 2023-09-04T11:45:59Z

Publisher:

Published
DOI:10.1109/TED.2023.3265626

Terms of use:
The institutional repository of the University of Udine (http://air.uniud.it) is provided by ARIC services. The aim is to enable open access to all the world.

Publisher copyright

(Article begins on next page)

29 April 2024

Analytical procedure for the extraction of material parameters in antiferroelectric ZrO_2

Mattia Segatto *Graduate Student Member, IEEE*, Filippo Rupil, and David Esseni *Fellow, IEEE*,

Abstract

We here present an analytical procedure to extract the anisotropy constants of antiferroelectric materials from a few key features of the experimental polarization versus field curves. Our approach is validated for two experimental data sets of ZrO_2 capacitors, and the extracted parameters are consistent with the microscopically non-polar nature of the zero field state of the antiferroelectric ZrO_2. The methodology has applications in antiferroelectric non-volatile memories and memristors, as well as in electron devices exploiting the negative capacitance operation of ZrO_2.

Index Terms

Ferroelectricity, Antiferroelectricity, Zirconium Oxide, Negative Capacitance

© 2023 IEEE. Personal use of this material is permitted. Permission from IEEE must be obtained for all other uses, in any current or future media, including reprinting/republishing this material for advertising or promotional purposes, creating new collective works, for resale or redistribution to servers or lists, or reuse of any copyrighted component of this work in other works.

I. Introduction

Antiferroelectric materials are already employed in a wide range of applications such as energy storage capacitors, electrical actuators and non-volatile memories [1]. In fact, antiferroelectric materials promise a few advantages over ferroelectric materials for memory applications. For example, ferroelectric hafnium oxides have a high coercive field that tends to reduce the cycling endurance [2]–[5]. Antiferroelectric materials, instead, have shown better endurance properties [6], that have been attributed to a smaller electrical stress due to the fact that one of the two memory states is non-polar [5], to a lower charge injection [7], as well as to different switching mechanisms [7], [8].

In most perovskites, such as $PbZrO_3$, antiferroelectricity has been ascribed to a macroscopically non-polar ground state stemming from the anti-polar alignment of polar domains [10], [11], which can be re-aligned by the application of an electric field. This is the physical picture behind the phenomenological Kittel's model of antiferroelectricity [12]. A more pragmatic compact model for antiferroelectric capacitors can be also based on the nucleation limited switching approach [13], or on the Preisach's model [14]. Recently the antiferroelectric behaviour has been also

This work was supported in part by the European Union H2020 under Grant GA:871737.

M. Segatto and D. Esseni are affiliated to the Polytechnic Department of Engineering and Architecture (DPIA) at University of Udine, Via delle Scienze 206, Udine, Italy. F. Rupil is currently a student at University of Udine.

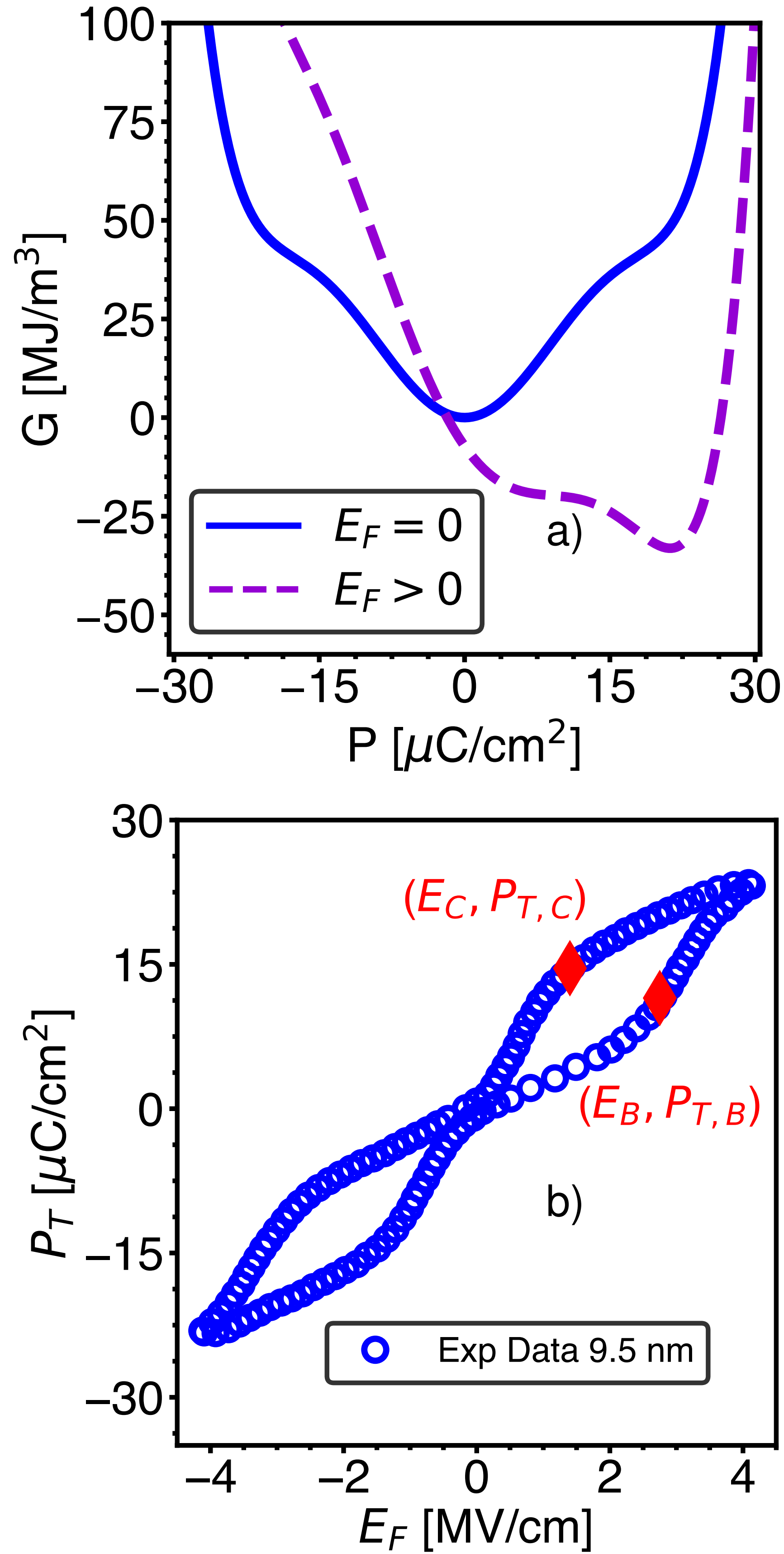

Fig. 1: a) Gibbs' free energy landscapes calculated from Eq. (1) with the anisotropy constants in Table I, and for either a zero or a positive applied field E_F. At zero field (blue curve) the point E_F=P=0 is a free energy minimum and thus it is a stable steady-state point for the system. The application of a positive E_F (purple curve) shifts the energy minimum to a positive P. b) Measured total polarization versus applied electric field in a TiN/ZrO_2(9.5 nm)/TiN stack [9]. The meaning of points B and C is discussed in the text.

observed in hafnium and zirconium based materials [15], which exhibit also ferroelectricity and are of great interest due to their scalability and CMOS process compatibility. The microscopic picture behind antiferroelectricity in ZrO_2 is fundamentally different compared to $PbZrO_3$ and similar perovskites. In fact *ab-initio* calculations have revealed that the energy ground state of thin ZrO_2 films is tetragonal [16], which has been also confirmed by GIXRD measurements [5], [15], [17], so that at zero applied field the material is microscopically non-polar [16], [18]. By applying an electric field to the ZrO_2, a phase transition is induced from the non-polar tetragonal phase to a polar orthorombic phase, which is the phase also responsible for ferroelectricity in Hafnium-Zirconium Oxides (HZOs).

While Kittel's model gives an adequate description for antiferroelectric materials having an anti-polar alignment of the domains, it may not be suitable to describe the physical picture governing the antiferroelectricity in ZrO_2, which, as stated before, is quite different from the one observed in perovskites. In this paper we propose a procedure to extract the material parameters of the antiferroelectric ZrO_2 in the framework of the multi–domain Landau, Ginzburg, Devonshire (LGD) model, that can be applied to antiferroelectric materials with microscopically non-polar ground state, such as ZrO_2. The calibrated LGD model can reproduce fairly well both the quasi-static polarization-field curves in [9], [17], and the transient negative capacitance behavior reported in [17]. Moreover, the parametrization of ZrO_2 is consistent with its microscopically non-polar state at zero applied field.

The paper is organized as follows. In Section II we propose a methodology to extract the anisotropy constants of the LGD model for an antiferroelectric material with non-polar ground state. In Section III we provide a quick overview of the simulation framework used to validate the proposed extraction procedure. In Section IV, we show comparisons between simulations and experiments for different ZrO_2 thicknesses and operation regimes. In Section V we offer a few concluding remarks.

II. Extraction of anisotropy constants

Let us here consider a capacitor with metal electrodes and a ferroelectric (FE) or anti-ferroelectric (AFE) dielectric. For a simple homogeneous polarization picture, the Gibbs' free energy of the system consisting of the capacitor and the external battery can be written as [19]

$$G = \alpha P^2 + \beta P^4 + \gamma P^6 - E_F\, P - \frac{\varepsilon_0 \varepsilon_F E_F^2}{2} \tag{1}$$

where ε_0 is the vacuum permittivity, P, ε_F, E_F are the spontaneous polarization, background permittivity and electric field of the FE or AFE material, while α, β and γ are the anisotropy constants. The quasi-static P-E_F trajectories are identified by the conditions (dG/dP)=0 and (d^2G/dP^2)>0, [20], namely

$$2\alpha P + 4\beta P^3 + 6\gamma P^5 = E_F \tag{2a}$$

$$\frac{\partial E_F}{\partial P} = 2\alpha + 12\beta P^2 + 30\gamma P^4 \geq 0 \tag{2b}$$

Quasi-static experiments in a metal-FE-metal or metal-AFE-metal stack probe the overall charge in the system, usually denoted as total polarization $P_T \approx Q = P + \varepsilon_0 \varepsilon_F\, E_F$.

Figure 1a shows an example of the free energy landscape for a metal-AFE-metal (M-AFE-M) system, and Eq. (2) prescribes that α be positive in order to have a microscopically non-polar stable state at $E_F \approx 0$ and $P \approx 0$. Figure 1b displays the experimental P_T versus E_F curve recently reported for a ZrO_2 capacitor [9]. In Fig. 1b we denote by E_B, E_C the coercive fields corresponding respectively to the non-polar to positive and positive to non-polar transition in the $P_T - E_F$ curve. In practice, the points (E_B, $P_{T,B}$) and (E_C, $P_{T,C}$) can be identified as the points where the P_T versus E_F curve exhibits a clear change in the slope. In order to define an analytical procedure for the extraction of material parameters in antiferroelectric ZrO2, we now assume that points B and C correspond respectively to a maximum and a minimum of the static $E_F - P_T$ relation implied by the LGD polynomial. In Appendix I, we show that such maximum and minimum of the $E_F - P_T$ relation coincide with those of the $E_F - P$ relation, which in turn are readily identified by the condition $(\partial E_F/\partial P) = 0$ in Eq. (2b). Hence, the conditions ensuring that the quasi-static P_T-E_F trajectories include points B and C become

$$2\alpha \quad + 12\beta\, P_C^2 + 30\gamma\, P_C^4 = 0 \tag{3a}$$

$$2\alpha\, P_C + 4\beta\, P_C^3 \quad + 6\gamma\, P_C^5 \quad = E_C \tag{3b}$$

$$2\alpha \quad + 12\beta\, P_B^2 + 30\gamma\, P_B^4 = 0 \tag{3c}$$

$$2\alpha\, P_B + 4\beta\, P_B^3 \quad + 6\gamma\, P_B^5 \quad = E_B \tag{3d}$$

From Eqs. (3a) to (3c) we can readily express α, β, γ as

$$\alpha = \frac{3}{4}\frac{E_C}{P_C} + \frac{3}{4}\frac{E_C P_C}{5P_B^2 - P_C^2} \tag{4a}$$

$$\beta = -\frac{E_C}{8P_C^3} - \frac{3}{4}\frac{E_C}{P_C\,(5P_B^2 - P_C^2)} \tag{4b}$$

$$\gamma = \frac{E_C}{4P_C^3\,(5P_B^2 - P_C^2)} \tag{4c}$$

Eq. (4) provides the anisotropy constants in terms of E_C, P_C, P_B. However, the spontaneous polarizations P_C, P_B cannot be directly identified in the experimental curves of Figure 1b, but they must be calculated by using P=$P_T - \varepsilon_F\varepsilon_0\, E_F$. This implies that the α, β, γ in Eq. (4) are given in terms of E_C, $P_{T,C}$, $P_{T,B}$ and of the remaining parameter ε_F. In this latter respect, it has been theoretically argued that ε_F should be considered an adjustable parameter rather a true material constant [21], and in practice it is difficult to extract ε_F independently of α, β, γ. Therefore, we now substitute α, β, γ from Eq. (4) into Eq. (3d) and rearrange it as

$$\frac{P_C^3(5P_B^2 - P_C^2)}{P_B^3(5P_C^2 - P_B^2)} = \frac{E_C}{E_B} \tag{5}$$

By recalling P_C=$P_{T,C} - \varepsilon_0\varepsilon_F\, E_C$ and P_B=$P_{T,B} - \varepsilon_0\varepsilon_F\, E_B$, Eq. (5) can now be solved for ε_F. Namely ε_F can be used as the fourth adjustable parameter determined by Eqs. (3), so as to ensure that the quasi-static P_T-E_F trajectories include the points B and C in Fig. 1b.

As it can be seen, Eq. (5) implies also $(5P_B^2{-}P_C^2){>}0$ (because $5P_C^2$ is by definition larger than P_B^2), which in turn results in positive α, γ values and in a negative β value (see Eq. (4)). As already mentioned, the positive α value is consistent with the microscopically non-polar nature of thin ZrO_2 films at a zero applied field and it is also

consistent with previous literature for antiferroelectric ZrO_2 [22], [23]. Moreover, a positive α value is the only possible choice in order to obtain no remnant polarization.

In summary, the procedure to extract the anisotropy constants from experiments requires to firstly identify the points B and C in the measured P_T-E_F curves (see Fig. 1b). Then Eq. (5) can be solved numerically to determine ε_F and, once ε_F is known, Eq. (4) provides expressions for α, β, γ.

III. Framework for numerical modelling

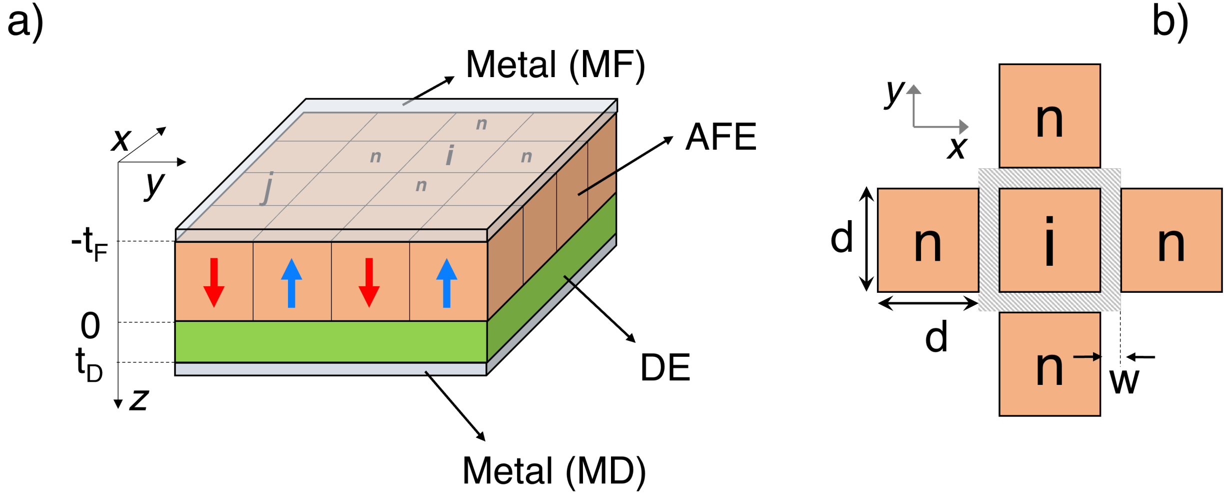

Fig. 2: Sketch of a device structure corresponding to a metal-AFE-dielectric-metal stack. a) sketch showing thickness t_F of the AFE layer, the thickness t_D of the dielectric (DE), and the partition of the AFE layer in n_D domains. b) focus on the nearest neighbour domains included in the sum over n in Eq. (6), and describing the domain wall energy contribution. d and w denote respectively the domain size and the width of the domain wall region [19].

In Section IV we will illustrate several comparisons between simulations and experiments aimed at a validation of the extraction procedure for the anisotropy constants of ZrO_2. All simulations were carried out by using the solver for the multi-domain LGD equations that has been already discussed in [19], [24], [25]. In this section we recall only a few aspects of the simulation framework, which are relevant for the cases at study in this paper. For an AFE or a ferroelectric material consisting of n_D domains as shown in Fig. 2, the dynamics of the polarization P_i in each domain is described by equations [19], [24], [25]

$$\begin{aligned}\frac{\partial P_i}{\partial t} &= \frac{1}{t_F\,\rho}[-\left(2\alpha_i\,P_i + 4\beta_i\,P_i^3 + 6\gamma_i\,P_i^5\right)t_F + \\ &- \frac{t_F\,k}{d\,w}\sum_n (P_i - P_n) - \sum_{j=1}^{n_D} P_j/C_{i,j}^{(dep)} + (C_D/C_0)V_T]\end{aligned} \tag{6}$$

where k is the domain wall coupling coefficient, ρ is the switching resistivity, while $1/C_{i,j}^{(dep)}$=$1/2(1/C_{j,i}+1/C_{i,j})$ and the terms $C_{i,j}$ are the capacitive couplings between domains. Given the similarity between the crystal chemistry of ZrO_2 and HfO_2 [26], in simulations we used $k \approx 0$, as suggested by recent first principle calculations for HfO_2 [27]. For each domain, the α_i, β_i, γ_i values were calculated by using a Gaussian distribution of the coercive fields

with the mean E_C, E_B values used to extract the parameters in Table I, and with a ratio $\sigma_{EC} = \sigma_{EB}$ between the standard deviation and mean value; ε_F is the same in all domains. All simulations were performed using $n_D = 400$ domains with a domain area of 25 nm^2. The number of domains n_D mainly influences the number of terms $1/C_{i,j}^{(dep)}$ which, as stated before, describe the capacitive coupling between the $i-$th and $j-$th domain. However, such a capacitive coupling decreases quite steeply with the distance between domains, so that simulations become insensitive to n_D for large enough n_D values. Moreover, for a M-AFE-M stack (without the DE layer in Fig. 2) the terms $1/C_{i,j}^{(dep)}$ tend to zero because there is no electrostatic coupling between the domains through the dielectric layer, which further reduces the sensitivity to n_D of the simulations results. The experimental P_T versus E_F curves for AFE ZrO_2 sometimes exhibit a non negligible polarization at zero field, that is ascribed to the presence of ferroelectric domains. Therefore, in our simulations, we accounted for a small fraction of ferroelectric domains, which can be included in our model by setting appropriate values of the anisotropy constants for such domains. More precisely, for the LGD parametrization of ferroelectric domains in ZrO_2 we used educated guesses for the remnant polarization $P_r \simeq 25$ μC/cm^2 and coercive field $E_{C,FE} \simeq 1.2$ MV/cm consistent with [28], [29], resulting in the following LGD parametrization: $\alpha_{FE} = -5.94 \cdot 10^8$ m^3/F, $\beta_{FE} = 4.28 \cdot 10^9$ m^5/(FC^2) and $\gamma_{FE} = 1.16 \cdot 10^9$ m^9/(FC^4).

Even for ferroelectric domains we introduced a Gaussian distribution of the coercive field, with the same σ_{EC} value used for antiferroelectric domains. The domain dependent anisotropy constants have a spatially random distribution across the domain grid, and we have verified that their spatial distribution does not practically affect the simulation results. This is not unexpected especially for M-AFE-M stacks, where there is no electrostatic coupling between the domains. In our simulations it is also possible to include a small built-in electric field in the ferroelectric material, possibly arising from a slight workfunction difference at the two electrodes or from fixed charges in the dielectric stack.

IV. Comparison with experimental results

	α [m/F]	β [m^5/(FC^2)]	γ [m^9/(FC^4)]	ε_F [-]	t_{ZrO_2} [nm]	E_{BI} [kV/cm]
[9]	$3.37 \cdot 10^9$	$-1.57 \cdot 10^{11}$	$3.24 \cdot 10^{12}$	23.76	5.3	0
[9]	$3.56 \cdot 10^9$	$-2.01 \cdot 10^{11}$	$4.50 \cdot 10^{12}$	22.09	9.5	-50
[17]	$2.95 \cdot 10^9$	$-8.97 \cdot 10^{10}$	$1.09 \cdot 10^{12}$	13.36	10	50

TABLE I: Nominal values of the parameters extracted from Eqs. (4) and (5) for experiments from [9] and [17]. E_{BI} denotes a built-in electric field; the switching resistivity $\rho \sim 400$ Ωm was used in all simulations.

Table I reports the material parameters extracted with the methodology of this work from two experimental data sets, namely the P_T-E_F curves recently reported in [9] and [17]. Quite interestingly, from the parameters in Table I

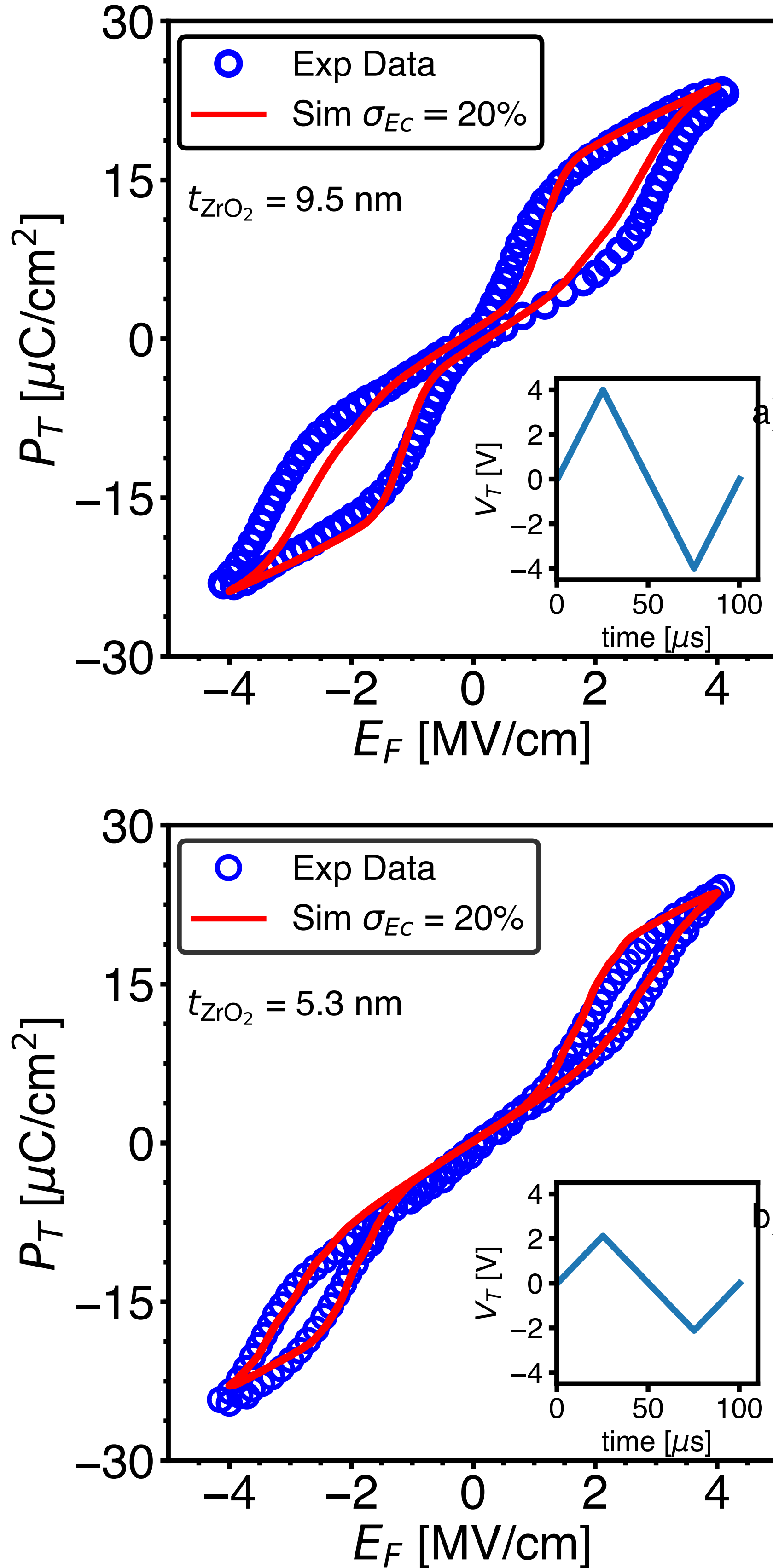

Fig. 3: Comparison between simulations and experiments for quasi-static P_T versus E_F curves of the TiN/ZrO_2/TiN capacitors from [9]. The triangular voltage waveforms at a 10 kHz frequency are shown in the insets. a) Thickness of the ZrO_2 layer $t_{ZrO_2} = 9.5$ nm, points used for parameters extraction: (E_B, $P_{T,B}$) = (2.7 MV/cm, 9.5 μC/cm^2); (E_C, $P_{T,C}$) = (1.1 MV/cm, 14.5 μC/cm^2). b) $t_{ZrO_2} = 5.3$ nm, (E_B, $P_{T,B}$) = (2.9 MV/cm, 14 μC/cm^2); (E_C, $P_{T,C}$) = (2.4 MV/cm, 16 μC/cm^2).

one can calculate the zero field permittivity of ZrO_2, which is defined as $1/\varepsilon_0(\partial P_T/\partial E_F)$ at E_F=P_T=0. By recalling P_T=P+$\varepsilon_0\varepsilon_F\,E_F$ and using Eq. (2a) for $(\partial P/\partial E_F)$, the zero-field permittivity is readily expressed as $(\varepsilon_F + 1/(2\alpha\varepsilon_0))$. As already mentioned in Section II, while ε_F is related to the zero-field permittivity, which is the quantity actually measured in experiments, it is not equivalent to it and can be thought as a fitting parameter [21].

The zero field permittivity obtained from the parameters in Table I ranges between 30 and 40, which is in good agreement with experimental values in [30], [31]. The anisotropy constants in Table I provide the mean values of the domain dependent α_i, β_i, γ_i parameters used in the numerical simulations.

In Fig. 3 we show a comparison between simulations and experiments for the P_T−E_F curves of the M-AFE-M stacks reported in [9], and for the materials parameters in Table I. In Fig. 3a we considered 3% of the overall domains to be ferroelectric with the parameters discussed in Section III, while for Fig. 3b we didn't include ferroelectric domains as it can be seen that the hysteresis of the $P_T - E_F$ curve is completely closed at zero applied electric field.

In our model, the timescale for the polarization dynamics is $t_\rho = \rho/(2\langle\alpha\rangle)$ [24]. For $\rho \approx 400\ \Omega m$ (see Table I) we have $t_\rho \approx 70$ ns, which is consistent with the literature for large area devices [32], and ensures that simulations in Fig. 3 are quasi-static. While it could be argued that each stack could have its own ρ value, there is no direct measurement to extract it, rather it is usually inferred from polarization switching measurements [33]. Given the lack of a direct information about the value of ρ, we kept its value fixed for all stacks. The agreement between simulations and experiments is fairly good for both t_{ZrO_2} values, thanks to a good symmetry of the experiments along both the P_T and E_F axis.

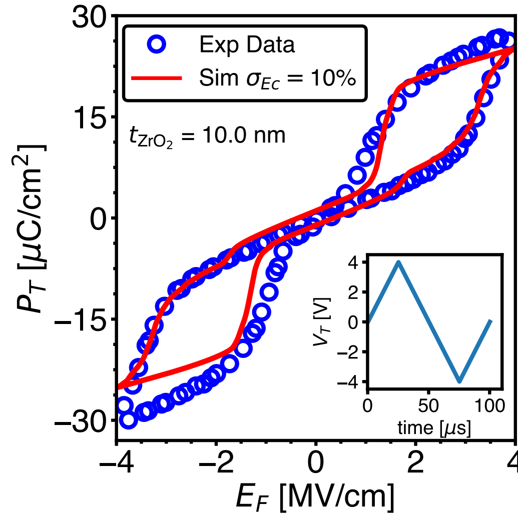

Fig. 4: Comparison between simulations and experiments for quasi-static P_T versus E_F curves of a TiN/ZrO_2/TiN capacitor from [17]. The triangular voltage waveforms at a 10 kHz frequency are shown in the inset. (E_B, $P_{T,B}$) = (3.1 MV/cm, 12 μC/cm^2); (E_C, $P_{T,C}$) = (1.6 MV/cm, 18 μC/cm^2).

Fig. 4 reports a similar comparison for the experimental data set in [17], where we considered 4% of the domains

to be ferroelectric. The agreement between simulations and experiments is still fairly good, but we also observe a discrepancy in the negative E_F hysteresis. This is mainly due to an asymmetry in the measured P_T values for positive and negative E_F at large $|E_F|$, possibly due to a non negligible influence of leakage. In fact, while an asymmetry along the E_F axis can be included in our model through a built-in field E_{BI} (see Table I), the LGD model is instead inherently symmetric in the P_T values.

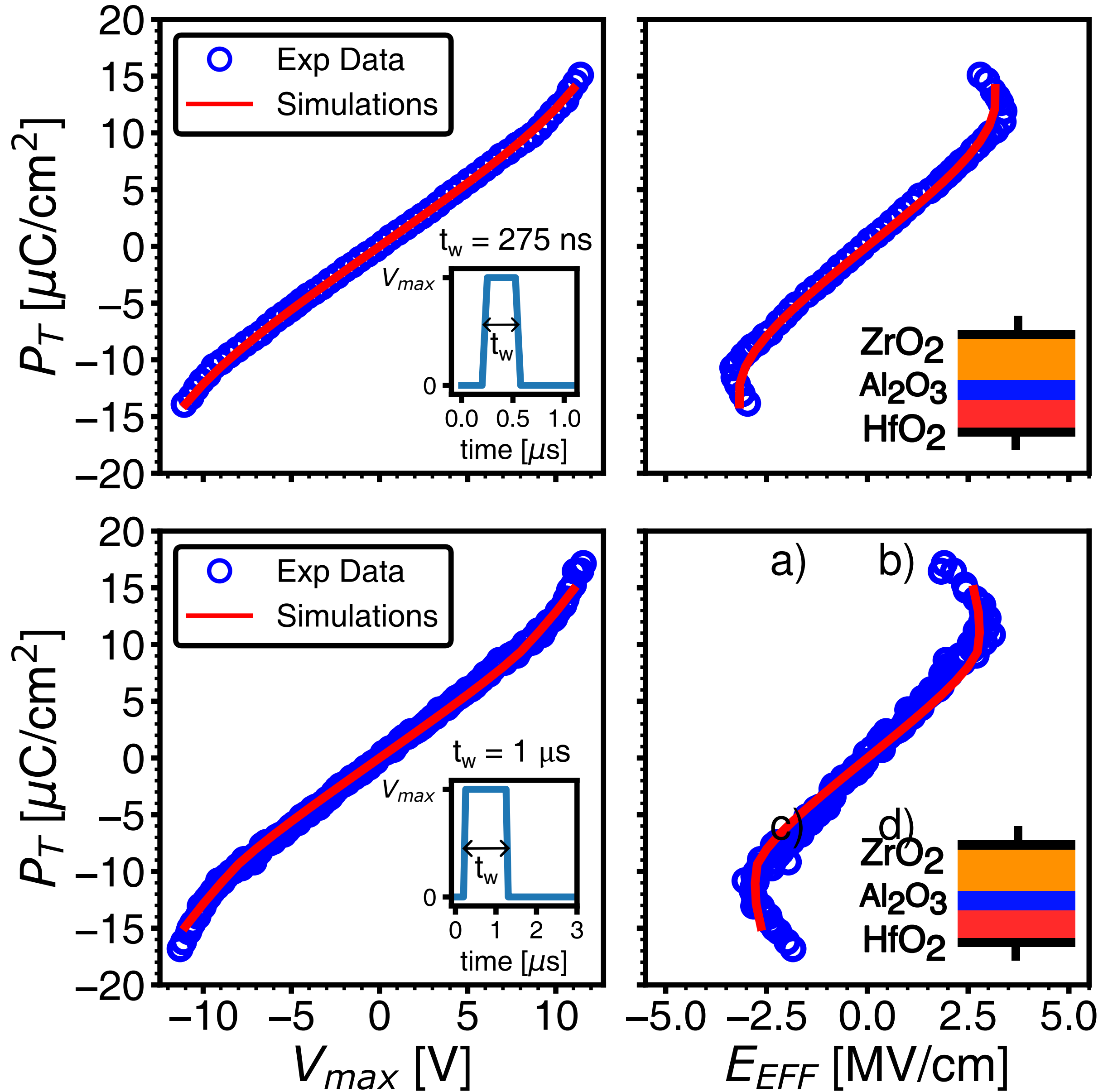

Fig. 5: Comparison between simulations and experiments for transient negative capacitance measurements in a TiN/ZrO_2/Al_2O_3/HfO_2/TiN capacitor [17]. (a, c) P_T versus V_{max} curve for pulsed measurements with pulse width of 275 ns and 1 μs, respecitvely. (b, d) Corresponding P_T versus effective field, E_{EFF}, curve.

The authors of [17] also reported transient negative capacitance (NC) experiments, that we here analyse by

using the LGD model, as previously reported for the NC behaviour in ferroelectric devices [24], [34]–[36]. In the TiN/ZrO_2/Al_2O_3/HfO_2/TiN stack the undoped HfO_2 layer is paraelectric and the thicknesses are: $t_{\mathrm{ZrO_2}} = 10$ nm, $t_{\mathrm{Al_20_3}} \approx 1$ nm and $t_{\mathrm{HfO_2}} = 8$ nm. The timescale of the voltage pulses in these experiments (now comparable to the t_ρ), and the relatively thick dielectric were on purposely chosen to minimize the role of charge injection and trapping [17]. Therefore, our simulations neglect trapping, which has been shown to be instead important in quasi-static measurements for FE-oxide stacks having a thin dielectric layer [25], [37]. Figure 5a and 5c compare the simulated and experimental $P_T - V_{max}$ curves for a pulse width of respectitvely of 275 ns and 1 μs, where V_{max} is the amplitude of the voltage pulse and the simulated P_T values have been extracted following the definition in [17]. Figure 5b and 5d display the corresponding plots for the P_T versus an effective electric field, E_{EFF}, across the ZrO_2 layer. In experiments the E_{EFF} cannot be directly probed, hence it was estimated as $E_{EFF} \approx (V_{max} - P_T/C_D)/t_{\mathrm{ZrO_2}}$, where C_D≈1.78 μF/cm^2 is the effective capacitance of the Al_2O_3-HfO_2 series [17]. In the simulations of Fig. 5b and 5d, the E_{EFF} was calculated according to the same definition given in [17]. Figure 5 shows that the same ZrO_2 parameters already employed in Fig. 4, both LGD mean values and their statistical distribution, can provide a fairly good agreement also for transient NC experiments, with a matching between simulations and experiments that is similarly good for the two different pulse widths. The results in Figure 5 reinforce our confidence in the extraction procedure for the ZrO_2 parameters and in the overall simulation framework.

V. Discussion and conclusions

We have proposed a procedure to extract the material parameters for the LGD model of antiferroelectric ZrO_2 films, which is consistent with the microscopically non-polar nature of the zero field state in antiferroelectric ZrO_2 [17]. The points (E_B, $P_{T,B}$) and (E_C, $P_{T,C}$) necessary to extract the anisotropy constants can be reliably identified by a distinct change in P_T versus E_F slope of the $P_T - E_F$ curves (see Fig. 1b), provided that the curves are not significantly distorted by leakage and that they display a full hysteresis loop, as opposed to minor loops. Our methodology was successfully validated by considering quasi-static $P_T - E_F$ curves in M-AFE-M stacks, where a small fraction of ferroelectric domains was also included in the model to explain and reproduce the residual polarization at zero field observed in some AFE ZrO_2 films [9]. Moreover, we analysed very recent experiments reporting both $P_T - E_F$ curves in M-AFE-M stacks and transient negative capacitance experiments in a TiN/ZrO_2/Al_2O_3/HfO_2/TiN stack. With a single set of ZrO_2 parameters extracted from the $P_T - E_F$ curves, our simulations could reproduce fairly well also the transient negative capacitance experiments and for different pulse widths.

Our analytical extraction procedure has a clear physical background and it is easy to implement, although it may lead to fitting results that are not as accurate as those obtained with more phenomenological approaches [13], [14], where the quite many parameters of the models are typically extracted by using numerical procedures targeting a minimization of the mean squared error between simulations and experiments.

We believe that the methodology proposed in this paper to extract the anisotropy constants of antiferroelectic ZrO_2 layers will have useful applications in ferroelectric non-volatile memories and memristors, as well as in

possible devices exploiting the ZrO2 negative capacitance behavior.

Appendix A

In order to show that the maximum and minimum of the static $E_F - P_T$ curve coincide with those of the $E_F - P$ curve, we can substitute $P = P_T - \varepsilon_0\varepsilon_F E_F$ in Eq. (2a) and obtain

$$\begin{aligned} E_F =& 2\alpha\left(P_T - \varepsilon_0\varepsilon_F E_F\right) + +4\beta\left(P_T - \varepsilon_0\varepsilon_F E_F\right)^3 + \\ &+6\gamma\left(P_T - \varepsilon_0\varepsilon_F E_F\right)^5 \end{aligned} \tag{7}$$

Then, we derive both sides of Eq. (7) with respect to P_T and we have

$$\begin{aligned} \frac{\partial E_F}{\partial P_T} =& 2\alpha\left(1 - \varepsilon_0\varepsilon_F E_F\frac{\partial E_F}{\partial P_T}\right) + \\ &+12\beta\underbrace{\left(P_T - \varepsilon_0\varepsilon_F E_F\right)^2}_{P^2}\left(1 - \varepsilon_0\varepsilon_F E_F\frac{\partial E_F}{\partial P_T}\right) \\ &+30\gamma\underbrace{\left(P_T - \varepsilon_0\varepsilon_F E_F\right)^4}_{P^4}\left(1 - \varepsilon_0\varepsilon_F E_F\frac{\partial E_F}{\partial P_T}\right) \end{aligned} \tag{8}$$

which can be refactored in

$$\begin{aligned} &\frac{\partial E_F}{\partial P_T}\left[1 + \varepsilon_0\varepsilon_F(2\alpha + 12\beta P^2 + 30\gamma P^4)\right] = \\ &= 2\alpha + 12\beta P^2 + 30\gamma P^4 \end{aligned} \tag{9}$$

Equation (9) clearly shows that the condition

$$\frac{\partial E_F}{\partial P} = 2\alpha + 12\beta P^2 + 30\gamma P^4 = 0 \tag{10}$$

implies also $(\partial E_F/\partial P_T) = 0$.

Acknowledgment

Authors are thankful to Daniel Lizzit, Riccardo Fontanini and Marco Massarotto for fruitful discussions, and to Michael Hoffmann for sharing experimental data of [17].

References

[1] C. A. Randall, Z. Fan, I. Reaney, L.-Q. Chen, and S. Trolier-McKinstry, “Antiferroelectrics: History, fundamentals, crystal chemistry, crystal structures, size effects, and applications,” *Journal of the American Ceramic Society*, vol. 104, no. 8, pp. 3775–3810, 2021. [Online]. Available: https://ceramics.onlinelibrary.wiley.com/doi/abs/10.1111/jace.17834

[2] E. Yurchuk, S. Mueller, D. Martin, S. Slesazeck, U. Schroeder, T. Mikolajick, J. Müller, J. Paul, R. Hoffmann, J. Sundqvist, T. Schlösser, R. Boschke, R. van Bentum, and M. Trentzsch, “Origin of the endurance degradation in the novel HfO_2-based 1T ferroelectric non-volatile memories,” in *2014 IEEE International Reliability Physics Symposium*, 2014, pp. 2E.5.1–2E.5.5.

[3] M. Pesic, F. P. G. Fengler, S. Slesazeck, U. Schroeder, T. Mikolajick, L. Larcher, and A. Padovani, “Root cause of degradation in novel HfO_2-based ferroelectric memories,” in *2016 IEEE International Reliability Physics Symposium (IRPS)*, 2016, pp. MY–3–1–MY–3–5.

[4] M. Pešić, F. P. G. Fengler, L. Larcher, A. Padovani, T. Schenk, E. D. Grimley, X. Sang, J. M. LeBeau, S. Slesazeck, U. Schroeder, and T. Mikolajick, “Physical Mechanisms behind the Field-Cycling Behavior of HfO_2-Based Ferroelectric Capacitors,” *Advanced Functional Materials*, vol. 26, no. 25, pp. 4601–4612, 2016. [Online]. Available: https://onlinelibrary.wiley.com/doi/abs/10.1002/adfm.201600590

[5] M. Pešić, M. Hoffmann, C. Richter, T. Mikolajick, and U. Schroeder, "Nonvolatile Random Access Memory and Energy Storage Based on Antiferroelectric Like Hysteresis in ZrO_2," *Advanced Functional Materials*, vol. 26, no. 41, pp. 7486–7494, 2016. [Online]. Available: https://onlinelibrary.wiley.com/doi/abs/10.1002/adfm.201603182

[6] M. H. Park, H. J. Kim, Y. J. Kim, T. Moon, K. D. Kim, and C. S. Hwang, "Thin $Hf_xZr_{1-x}O_2$ Films: A New Lead-Free System for Electrostatic Supercapacitors with Large Energy Storage Density and Robust Thermal Stability," *Advanced Energy Materials*, vol. 4, no. 16, p. 1400610, 2014. [Online]. Available: https://onlinelibrary.wiley.com/doi/abs/10.1002/aenm.201400610

[7] X. J. Lou, "Why do antiferroelectrics show higher fatigue resistance than ferroelectrics under bipolar electrical cycling?" *Applied Physics Letters*, vol. 94, no. 7, p. 072901, 2009. [Online]. Available: https://doi.org/10.1063/1.3082375

[8] L. Zhou, R. Z. Zuo, G. Rixecker, A. Zimmermann, T. Utschig, and F. Aldinger, "Electric fatigue in antiferroelectric ceramics induced by bipolar electric cycling," *Journal of Applied Physics*, vol. 99, no. 4, p. 044102, 2006. [Online]. Available: https://doi.org/10.1063/1.2172725

[9] X. Luo, K. Toprasertpong, M. Takenaka, and S. Takagi, "Antiferroelectric properties of ZrO_2 ultra-thin films prepared by atomic layer deposition," *Applied Physics Letters*, vol. 118, no. 23, p. 232904, 2021. [Online]. Available: https://doi.org/10.1063/5.0051068

[10] E. Sawaguchi, H. Maniwa, and S. Hoshino, "Antiferroelectric Structure of Lead Zirconate," *Phys. Rev.*, vol. 83, pp. 1078–1078, Sep 1951. [Online]. Available: https://link.aps.org/doi/10.1103/PhysRev.83.1078

[11] A. N. Morozovska, E. A. Eliseev, A. Biswas, N. V. Morozovsky, and S. V. Kalinin, "Effect of Surface Ionic Screening on Polarization Reversal and Phase Diagrams in Thin Antiferroelectric Films for Information and Energy Storage," *Phys. Rev. Applied*, vol. 16, p. 044053, Oct 2021. [Online]. Available: https://link.aps.org/doi/10.1103/PhysRevApplied.16.044053

[12] C. Kittel, "Theory of Antiferroelectric Crystals," *Phys. Rev.*, vol. 82, pp. 729–732, Jun 1951. [Online]. Available: https://link.aps.org/doi/10.1103/PhysRev.82.729

[13] C.-T. Tung, S. Salahuddin, and C. Hu, "A Compact Model of Antiferroelectric Capacitor," *IEEE Electron Device Letters*, vol. 43, no. 2, pp. 316–318, 2022.

[14] Z. Wang, J. Hur, N. Tasneem, W. Chern, S. Yu, and A. Khan, "Extraction of preisach model parameters for fluorite-structure ferroelectrics and antiferroelectrics," *Scientific Reports*, vol. 11, no. 1, p. 12474, Jun 2021. [Online]. Available: https://doi.org/10.1038/s41598-021-91492-w

[15] J. Müller, T. S. Böscke, U. Schröder, S. Mueller, D. Bräuhaus, U. Böttger, L. Frey, and T. Mikolajick, "Ferroelectricity in Simple Binary ZrO_2 and HfO_2," *Nano Letters*, vol. 12, no. 8, pp. 4318–4323, 2012, pMID: 22812909. [Online]. Available: https://doi.org/10.1021/nl302049k

[16] S. E. Reyes-Lillo, K. F. Garrity, and K. M. Rabe, "Antiferroelectricity in thin-film ZrO_2 from first principles," *Phys. Rev. B*, vol. 90, p. 140103, Oct 2014. [Online]. Available: https://link.aps.org/doi/10.1103/PhysRevB.90.140103

[17] M. Hoffmann, Z. Wang, N. Tasneem, A. Zubair, P. V. Ravindran, M. Tian, A. A. Gaskell, D. Triyoso, S. Consiglio, K. Tapily, R. Clark, J. Hur, S. S. K. Pentapati, S. K. Lim, M. Dopita, S. Yu, W. Chern, J. Kacher, S. E. Reyes-Lillo, D. Antoniadis, J. Ravichandran, S. Slesazeck, T. Mikolajick, and A. I. Khan, "Antiferroelectric negative capacitance from a structural phase transition in zirconia," *Nature Communications*, vol. 13, no. 1, p. 1228, Mar 2022. [Online]. Available: https://doi.org/10.1038/s41467-022-28860-1

[18] S. Lombardo, C. Nelson, K. Chae, S. Reyes-Lillo, M. Tian, N. Tasneem, Z. Wang, M. Hoffmann, D. Triyoso, S. Consiglio, K. Tapily, R. Clark, G. Leusink, K. Cho, A. Kummel, J. Kacher, and A. Khan, "Atomic-Scale Imaging of Polarization Switching in an (Anti-)Ferroelectric Memory Material: Zirconia (ZrO_2)," in *2020 IEEE Symposium on VLSI Technology*, 2020, pp. 1–2.

[19] T. Rollo, F. Blanchini, G. Giordano, R. Specogna, and D. Esseni, "Stabilization of negative capacitance in ferroelectric capacitors with and without a metal interlayer," *Nanoscale*, vol. 12,, pp. 6121–6129, 2020.

[20] T. Rollo and D. Esseni, "Energy Minimization and Kirchhoff's Laws in Negative Capacitance Ferroelectric Capacitors and MOSFETs," *IEEE Electron Device Letters*, vol. 38, no. 6, pp. 814–817, June 2017.

[21] A. P. Levanyuk, B. A. Strukov, and A. Cano, "Background dielectric permittivity: Material constant or fitting parameter?" *Ferroelectrics*, vol. 503, no. 1, pp. 94–103, 2016. [Online]. Available: https://doi.org/10.1080/00150193.2016.1218245

[22] P. D. Lomenzo, M. Materano, C. Richter, R. Alcala, T. Mikolajick, and U. Schroeder, "A Gibbs energy view of double hysteresis in ZrO_2 and Si-doped HfO_2," *Applied Physics Letters*, vol. 117, no. 14, p. 142904, 2020. [Online]. Available: https://doi.org/10.1063/5.0018199

[23] Y. Xu, Y. Yang, S. Zhao, T. Gong, P. Jiang, Y. Wang, P. Yuan, Z. Dang, Y. Chen, S. Lv, Y. Ding, Y. Wang, J. Bi, and Q. Luo, "Improved multibit storage reliability by design of ferroelectric modulated antiferroelectric memory," *IEEE Transactions on Electron Devices*, vol. 69, no. 4, pp. 2145–2150, 2022.

[24] D. Esseni and R. Fontanini, "Macroscopic and microscopic picture of negative capacitance operation in ferroelectric capacitors," *Nanoscale*, vol. 13, pp. 9641–9650, 2021.

[25] M. Segatto, R. Fontanini, F. Driussi, D. Lizzit, and D. Esseni, “Limitations to Electrical Probing of Spontaneous Polarization in Ferroelectric-Dielectric Heterostructures,” *IEEE Journal of the Electron Devices Society*, vol. 10, pp. 324–333, 2022.

[26] T. S. Böscke, J. Müller, D. Bräuhaus, U. Schröder, and U. Böttger, “Ferroelectricity in hafnium oxide thin films,” *Applied Physics Letters*, vol. 99, no. 10, p. 102903, 2011.

[27] H.-J. Lee, M. Lee, K. Lee, J. Jo, H. Yang, Y. Kim, S. C. Chae, U. Waghmare, and J. H. Lee, “Scale-free ferroelectricity induced by flat phonon bands in HfO_2,” *Science*, vol. 369, no. 6509, pp. 1343–1347, 2020. [Online]. Available: https://www.science.org/doi/abs/10.1126/science.aba0067

[28] R. Cao, Y. Wang, S. Zhao, Y. Yang, X. Zhao, W. Wang, X. Zhang, H. Lv, Q. Liu, and M. Liu, “Effects of capping electrode on ferroelectric properties of $Hf_{0.5}Zr_{0.5}O_2$ thin films,” *IEEE Electron Device Letters*, vol. 39, no. 8, pp. 1207–1210, 2018.

[29] B. S. Kim, S. D. Hyun, T. Moon, K. Do Kim, Y. H. Lee, H. W. Park, Y. B. Lee, J. Roh, B. Y. Kim, H. H. Kim, M. H. Park, and C. S. Hwang, “A Comparative Study on the Ferroelectric Performances in Atomic Layer Deposited $Hf_{0.5}Zr_{0.5}O_2$ Thin Films Using Tetrakis(ethylmethylamino) and Tetrakis(dimethylamino) Precursors,” *Nanoscale Research Letters*, vol. 15, no. 1, p. 72, Apr 2020. [Online]. Available: https://doi.org/10.1186/s11671-020-03301-4

[30] K. Kato, T. Saito, S. Shibayama, M. Sakashita, W. Takeuchi, N. Taoka, O. Nakatsuka, and S. Zaima, “Stabilized formation of tetragonal ZrO_2 thin film with high permittivity,” *Thin Solid Films*, vol. 557, pp. 192–196, 2014, the 8th International Conference on Silicon Epitaxy and Heterostructures (ICSI-8) and the 6th International Symposium on Control of Semiconductor Interfaces (ISCSI-VI). [Online]. Available: https://www.sciencedirect.com/science/article/pii/S0040609014000522

[31] J. Liu, J. Li, J. Wu, and J. Sun, “Structure and Dielectric Property of High-k ZrO_2 Films Grown by Atomic Layer Deposition Using Tetrakis(Dimethylamido)Zirconium and Ozone,” *Nanoscale Research Letters*, vol. 14, no. 1, p. 154, May 2019. [Online]. Available: https://doi.org/10.1186/s11671-019-2989-8

[32] M. Si, X. Lyu, P. R. Shrestha, X. Sun, H. Wang, K. P. Cheung, and P. D. Ye, “Ultrafast measurements of polarization switching dynamics on ferroelectric and anti-ferroelectric hafnium zirconium oxide,” *Applied Physics Letters*, vol. 115, no. 7, p. 072107, 2019. [Online]. Available: https://doi.org/10.1063/1.5098786

[33] M. Kobayashi, N. Ueyama, K. Jang, and T. Hiramoto, “Experimental Study on Polarization-Limited Operation Speed of Negative Capacitance FET with Ferroelectric HfO_2,” in *2016 IEEE International Electron Devices Meeting (IEDM)*, Dec 2016, pp. 314–317.

[34] M. Hoffmann, M. Gui, S. Slesazeck, R. Fontanini, M. Segatto, D. Esseni, and T. Mikolajick, “Intrinsic nature of negative capacitance in multidomain $Hf_{0.5}Zr_{0.5}O_2$-based ferroelectric/dielectric heterostructures,” *Advanced Functional Materials*, vol. 32, no. 2, p. 2108494, 2022. [Online]. Available: https://onlinelibrary.wiley.com/doi/abs/10.1002/adfm.202108494

[35] A. K. Saha and S. K. Gupta, “Multi-Domain Negative Capacitance Effects in Metal-Ferroelectric-Insulator-Semiconductor/Metal Stacks: A Phase-field Simulation Based Study,” *Scientific Reports*, vol. 10, no. 1, p. 10207, Jun 2020. [Online]. Available: https://doi.org/10.1038/s41598-020-66313-1

[36] A. K. Saha and S. K. Gupta, “Negative capacitance effects in ferroelectric heterostructures: A theoretical perspective,” *Journal of Applied Physics*, vol. 129, no. 8, p. 080901, 2021. [Online]. Available: https://doi.org/10.1063/5.0038971

[37] R. Fontanini, M. Segatto, K. S. Nair, M. Holzer, F. Driussi, I. Häusler, C. T. Koch, C. Dubourdieu, V. Deshpande, and D. Esseni, “Charge-Trapping-Induced Compensation of the Ferroelectric Polarization in FTJs: Optimal Conditions for a Synaptic Device Operation,” *IEEE Transactions on Electron Devices*, vol. 69, no. 7, pp. 3694–3699, 2022.